AIAA JOURNAL
Vol. 44, No. 12, December 2006

Three-Dimensional Computation of a Synthetic Jet in Quiescent Air

J. Cui* and R. K. Agarwal†
Washington University, St. Louis, Missouri 63130-4899

DOI: 10.2514/1.14213

An unsteady Reynolds-averaged Navier–Stokes solver, WIND, is employed to capture the flowfield features of a synthetic jet pulsing into the quiescent air, case 1 of NASA Langley Research Center Workshop: "CFD validation of synthetic jets and turbulent separation control," held at Williamsburg, Virginia in March 2004. Both 2-D and 3-D simulations of this case have been performed by employing the appropriate boundary conditions at diaphragm of the actuator. It should be noted that the computations reported in this paper strictly follow the guidelines of the workshop in terms of all the parameters and modeling issues such as grid resolution, time step, boundary conditions, turbulence modeling, etc. Furthermore, to authors' knowledge, this is the only paper among the workshop participants reporting the 3-D simulations for this case. Comparisons are made with the experimental data; fair agreement is obtained. It is shown that the unsteady Reynolds-averaged Navier–Stokes simulations are capable of predicting the overall features of the oscillatory synthetic jet flowfield; however, noticeable discrepancies remain between the computations and the experimental data.

Nomenclature

b	=	slot width ($b_{1/2}$ denotes the half-width of the slot)
D	=	diaphragm diameter
f	=	frequency of the synthetic jet
k	=	kinetic energy of turbulent fluctuations per unit mass
l	=	slot length
p	=	pressure
Re	=	jet Reynolds number, $U_J b\rho/(\pi\mu)$
S	=	jet Stokes number, $(\omega b\rho/\mu)^{1/2}$
Sr	=	jet Strouhal number, $2\pi f b_{1/2}/U_J$
T	=	temperature
U_J	=	maximum jet velocity
(u, v, w)	=	velocity components in (x, y, z) directions
(x, y, z)	=	Cartesian coordinates (x: along slot width, z: along slot length, y: normal to x–z plane)
μ	=	dynamic viscosity of air
ρ	=	density of air
ω	=	$2\pi f$

I. Introduction

RECENTLY, a promising approach to the control of wall-bounded as well as free-shear flows, using synthetic jet (the oscillating jet) actuators, has received a great deal of attention. A synthetic jet (SJ) actuator is driven by a piezoelectric diaphragm or a piston in a periodic manner with zero net mass-flux. A variety of impressive flow control results have been achieved experimentally including the vectoring of conventional propulsive jets, modification of aerodynamic characteristics of bluff bodies, control of lift and drag of airfoils by virtual aeroshaping, reduction of skin-friction of a flat plate boundary layer, enhanced mixing in circular jets, etc.

Presented as Paper 2222 at the 2nd AIAA Flow Control Conference, Portland, OR, 28 June–7 January 2004; received 25 October 2004; revision received 21 April 2006; accepted for publication 21 April 2006. Copyright © 2006 by J. Cui and R.K. Agarwal. Published by the American Institute of Aeronautics and Astronautics, Inc., with permission. Copies of this paper may be made for personal or internal use, on condition that the copier pay the $10.00 per-copy fee to the Copyright Clearance Center, Inc., 222 Rosewood Drive, Danvers, MA 01923; include the code $10.00 in correspondence with the CCC.

*Graduate Research Assistant, Department of Mechanical & Aerospace Engineering. Student Member AIAA.

†William Palm Professor of Engineering, Department of Mechanical & Aerospace Engineering. Fellow AIAA.

Kral et al. [1,2] performed the two-dimensional simulation of a synthetic jet by unsteady Reynolds-averaged Navier–Stokes (URANS) equations with boundary conditions applied at the orifice of the synthetic jet (not including the effect of the actuator cavity). For two adjacent synthetic jets, Guo et al. [3,4] have performed URANS computations with extensive parametric studies; the flow inside the actuator cavity was included in their simulations. Their results agreed with the experiments of Smith et al. [5,6] near the exits of the jets; however, the difference between the simulations and the experiments became greater in the far field away from the exits of the jets. Lee and Goldstein [7] performed the 2-D direct numerical simulation (DNS) of a synthetic jet. For studying the behavior of synthetic jets in crossflow, Mittal et al. [8] and Cui et al. [9] have performed the numerical simulations of the interaction of one and two synthetic jets, respectively, with a flat plate boundary layer. All these simulations were performed for 2-D synthetic jets emanating in quiescent air or in crossflow.

Rizzetta et al. [10] have investigated the flowfield of a 3-D rectangular slot synthetic jet by DNS. The geometric and flow parameters of the synthetic jet employed in their simulation were the same as those in the experiment of Smith and Glezer [11]. Their 2-D solutions produced velocity fluctuations that were significantly larger than the experimental values. However, the 3-D computations captured the spanwise instabilities that led to a breakup of the coherent vortex structures, comparing more favorably with the measured data; nevertheless the 3-D computations agreed only qualitatively with the experimental data. Lee and Goldstein [12] have also performed 3-D DNS to study the behavior of synthetic slot jets in microelectronic mechanical systems (MEMS) for altering the fine scale flow structures within a boundary layer. Their results showed that although the jets eliminated the targeted structures, new structures developed by blowing pulses of fluid resulting in 1–2% increase in overall drag. Recently, Kotapati and Mittal [13] have reported the 3-D DNS of the synthetic jet in quiescent air for NASA Langley Workshop Case 1 (the subject of this paper) by approximating the actual actuator cavity in the experiment with an equivalent rectangular cavity. Their conclusions for the time-averaged and phase-averaged flowfields are similar to those reported in this paper and by other workshop participants [14]. It should be noted that the paper by Kotapati and Mittal [13] also compares the turbulence statistics of the flow with the experimental data because the computations are based on DNS.

Several experimental studies have also been conducted for 2-D, axi-symmetric and 3-D synthetic jets with and without crossflow. Experiments for an isolated 2-D synthetic jet [5] and two adjacent

synthetic jets have been performed by Smith et al [5,6]. For an isolated axi-symmetric synthetic jet, experiments and computations have been performed by Ahmed and Bangash [15]. Recently experiments have been performed for circular and elliptic synthetic jets in crossflow by Zaman and Milanovic [16,17]. Honohan [18] has studied the interaction of slot synthetic jets with crossflow. NASA Langley Research Center [14] recently held a workshop on CFD validation of synthetic jets in March 2004. In the workshop, numerical results using a variety of computational methods and turbulence models were compared against the experimental data for three cases: 1) an isolated high aspect ratio rectangular synthetic slot jet emanating in quiescent air, 2) an axi-symmetric synthetic jet in crossflow, and 3) the separated flow behind a 2-D hump and its control with a steady and a synthetic jet. This paper presents the results of CFD validation for case 1 using the URANS CFD solver WIND.[‡]

II. Solution Methodology

CFD code WIND is a product of the NPARC Alliance [19],[‡] a partnership between the NASA Glenn Research Center (GRC) and the Arnold Engineering Development Center (AEDC). WIND computes the solution of the Navier–Stokes equations, along with the supporting equation sets for turbulent and chemically reacting flows by employing a variety of turbulence models and chemistry models, respectively. The governing equations are solved in conservation form and are discretized by employing an approximate-factorization scheme for both the viscous and inviscid flux terms. The right-hand side (RHS) of the discretized equations includes the known inviscid and viscous fluxes of second-order accuracy at current time step at time t. The left-hand side (LHS) contains the unknown "correction or perturbation" values of the flow variables obtained by linearization of the discrete governing equations about the flow variables at current time step. These linearized discrete equations for "perturbation values" of the flow variables are solved by employing an approximate-factorization scheme that results into a block tridiagonal system of equations in each of the three coordinate directions. The perturbation values of the flow variables when added to the solution at time t provide the solution at time $t + \mathrm{dt}$, where $\mathrm{dt} =$ time step. The spatial discretization of the inviscid fluxes is based on the second-order Roe scheme modified for stretched grids, whereas the viscous fluxes are second-order central-differenced on stretched grids. The time stepping is performed with an Euler implicit scheme. The overall accuracy of the algorithm is second-order for both steady-state and time-accurate computations.

There are several well-established ways to model the effects of turbulence in Navier-Stokes equations; these formulations differ in the way the turbulence is mathematically characterized and modeled. These formulations result in equations/approaches for solving turbulent flows known in the literature as URANS, large eddy simulation (LES), detached eddy simulation (DES), and DNS. The details of these approaches are not described here but can be obtained from the book by Wilcox [20] (for URANS, LES, and DNS) and [21,22] (for DES). In URANS, the flow variables are split into the time-averaged part and the turbulent fluctuation part resulting in the well-known "Reynolds Stresses," which are modeled by an eddy-viscosity multiplied by the strain tensor. The eddy-viscosity is determined by employing a "turbulence model." CFD code WIND supports several turbulence models including the Spalart–Allmaras (SA) one-equation model [23] and Menter's shear stress transport (SST) two-equation model [24]. Both SA and SST models are employed in the calculations reported in this paper.

A better approximation for computation of turbulent flows, compared with URANS equations, is the LES wherein the "filtered" Navier–Stokes equations are solved in conjunction with a simplified model for small-scale phenomena. In LES approach, the large eddies/structures in the turbulent flow are computed and only the filtered smaller eddies are modeled. The formulation results in a so-called subgrid scale stress tensor, which is modeled by defining a subgrid scale eddy-viscosity multiplied by the strain tensor. The most well-known subgrid scale turbulence model is the Smagorinsky model. LES computations require several orders of magnitude greater computational resources: both memory and CPU, compared with the URANS computations. As a result, at present, the LES computations remain resource prohibitive for 3-D simulations at high Reynolds numbers. In recent years, therefore, to retain the efficiency of URANS and accuracy of LES, hybrid URANS/LES models have been proposed especially for wall-bounded turbulent flows. The approach by Speziale [25] is the first attempt in this direction. He proposed to divide the subgrid scale eddy-viscosity into a mean and a fluctuating part. The fluctuating part of the subgrid scale eddy-viscosity is computed using a Smagorinsky type model, whereas the mean part of the eddy-viscosity is computed by multiplying the RANS eddy-viscosity by a transfer function. The transfer function itself is a functional of the integral of inertial range energy spectrum between the subgrid scale and the Kolmogorov scale. This function has an arbitrary exponent that requires calibration, but is constructed so as to become unity in the near wall region; thus a RANS model is recovered in a region close to the wall. Away from the wall, the eddy-viscosity described by the Speziale model reverts to provide LES type behavior.

In WIND, both the hybrid of SA model and LES [21] and the hybrid of SST model and LES [22] are available. The hybrid SA_LES model is referred to as DES model in WIND. The hybrid model reduces to the standard SST or SA model in high mean shear regions (e.g., near viscous walls), where the grid is refined and has a large aspect ratio unsuitable for LES model. As the grid is traversed away from the high mean shear regions, it typically becomes coarser and more isotropic; the hybrid model smoothly transitions to the LES model. These hybrid models are intended to improve the simulations for unsteady and massively separated flows [21,22]. The details of the SA_LES (DES) and SST_LES models are given in [21,22], respectively. In this paper, the computations are performed in 2-D and 3-D employing the SA, SST, SA_LES (DES), and SST_LES models. It should be noted that the participation in the workshop required selection of a single approach, for example, URANS with SA or SST model, LES with a subgrid scale model or hybrid URANS/LES approach, applied to a 2-D or 3-D simulation. This is the only paper in which both URANS with SA and SST models as well as URANS/LES approaches have been considered in both the 2-D and 3-D simulations with very careful implementation of the SJ boundary conditions ensuring that the net mass-flux over a jet cycle was close to zero.

III. Implementation Details

A. Actuator Configuration and Operating Conditions

The synthetic jet actuator used in the experiment is shown in Fig. 1 [17]. The actuator is a narrow cylindrical-shaped cavity connected through an orifice to a slot at the exit as shown in Fig. 1a. The width of the slot is $b = 1.27$ mm and its length $l = 35.56$ mm. The coordinate system is defined as follows: the origin is defined at the

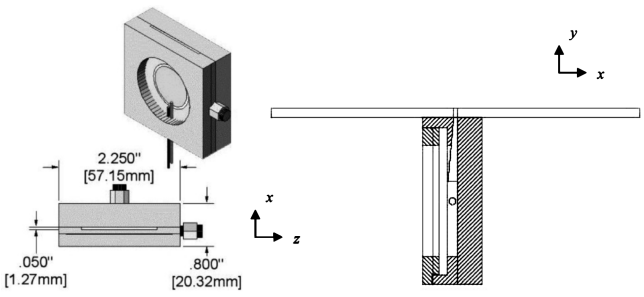

a) Diagram of the actuator b) Section at z = 0

Fig. 1 Configuration of the actuator [14].

[‡]Data available on-line at http://www.grc.nasa.gov/WWW/winddocs/user/index.html [cited 19 April 2004].

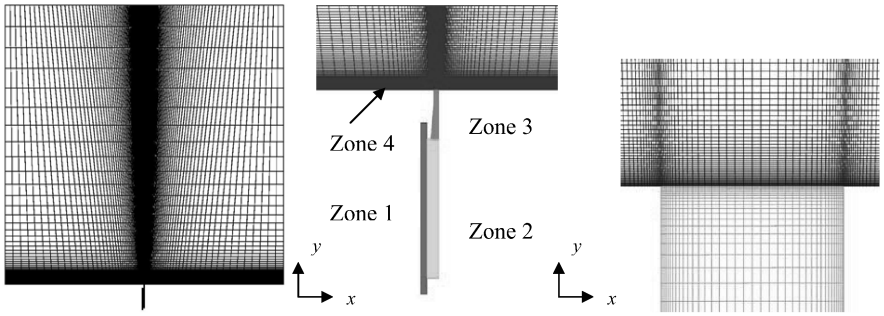

a) Whole grid **b) Configuration of four zones** **c) Grid in the slot (zone 3)**

Fig. 2 2-D grid used in the simulation.

center of the slot. The width of the slot is defined along the x-coordinate and z-coordinate is defined along the slot length, i.e., along the spanwise direction. Thus the jet is symmetric about $z = 0$. Figure 1b shows the section of the actuator mounted on a 3.175 mm thick square plate of dimensions 127×127 mm. The actuator is driven by a side-mounted piezoelectric diaphragm on the left side of the cavity. The diameter of the diaphragm is approximately 50.8 mm, which is clamped to the cavity by a 47 mm diameter O-ring. The actuator is flush-mounted on an aluminum plate at the floor and is covered by a cubic glass box of dimension 610 mm in all three (x, y, and z) directions and is 6.35 mm thick. The jet is located at the center of the floor of the box. The actuator operating parameters, which include diaphragm displacement, cavity pressure, and cavity temperature, were measured in the experiment; they provide boundary conditions for computations and actuator modeling. The following list provides jet operating conditions and other flow parameters. The flow medium is air.

1) $p = 101,325$ Pa
2) $T = 297$ K
3) $\rho = 1.185$ kg/m^3
4) $\mu = 1.84e-5$ kg/m $\cdot$ s
5) $D = 50.8$ mm
6) $f = 444.7$ Hz
7) $b = 1.27$ mm
8) $l = 35.56$ mm
9) $Re = 730$
10) $Sr = 0.063$
11) $S = 17$

B. 2-D Simulations: Mesh and Boundary Conditions

A two-dimensional zonal grid is generated by a code called zonal interactive graphics for grid generation (ZONI3G). Zonal connectivity information is computed by a preprocessing grid manipulation code (GMAN),[‡] and is stored in the grid file used by the WIND. During the course of a solution, WIND maintains continuity in flow properties across zone boundaries through a process known as zone coupling [26]. The 2-D grid for the actuator is generated based on the section at the symmetric plane, $z = 0$, shown in Fig. 1b. The external flow domain is 610×610 mm, same as the dimensions of the glass box used in the experiment. The computational mesh has four zones and 35,986 grid points. As shown in Fig. 2b, zone 1 is the left side of the cavity where the diaphragm is mounted, zone 2 is the right side of cavity, zone 3 is the orifice of width $b = 1.27$ mm, and zone 4 is the external flow domain. The number of grid points and the mesh spacing in each zone are given in Table 1. In the external flow region, the first grid above the floor is at a distance $\Delta y_{\min} = 0.00409$ mm. The y^+ is then calculated based on the shear stress along the floor of the long-time-averaged flowfield; y^+ is less than 1.7, which is sufficient to capture the turbulent character near the wall. Across the slot of the jet (in the x-direction), there are 41 points. The vortex structure has a dimension of about the same order as the slot width $b = 1.27$ mm. Thus the grid spacing in both x- and y-directions is enough to capture the travel of the propagation of unsteady vortical structure.

All the boundary conditions are also specified in GMAN, and are stored in the grid file used by WIND. In the external flow domain (zone 4), the bottom wall is no-slip from which the synthetic jet ejects into the quiescent air. The other three boundaries of zone 4 are specified as outflow boundaries. All the boundaries belonging to the cavity (zones 1, 2, and 3) are no-slip viscous walls, except the one where the diaphragm is located ($I = 1$, zone 1), where the "arbitrary inflow" boundary condition is specified as follows:

$$u(x, y = \text{const}, t) = U \sin(\omega t) \tag{1}$$

It should be noted that the "mode shape" of the piezoelectric diaphragm is not simulated. Instead, it is modeled as a "piston," with top-hat velocity profile, as a sinusoidal function of time. The volume change of the cavity is also not directly included directly in the simulation. The pressure at the diaphragm is first determined by averaging the pressure from the experimental measurement, which is 101,219 Pa. Using this value of the pressure at the diaphragm, it is found computationally that the net mass-flux over the slot during one jet cycle is not zero. It is found by numerical simulations that, for a relatively wide range of the forcing velocity of the diaphragm, the net mass-flux of the synthetic jet depends only on the pressure at the diaphragm and not on the excitation velocity. Therefore, this pressure at the diaphragm is tuned by calculating the mass-flux of the synthetic jet such that the net mass-flux over one jet cycle is close to zero. As shown in Fig. 3, when the pressure at the diaphragm is 101,419 Pa, the net mass-flux at the diaphragm is less than $1.0e-4$, and the net mass-flux at the synthetic jet slot is also less than $1.0e-2$. After this pressure at the diaphragm is determined computationally, the velocity amplitude of the jet at the exit depends only on the velocity amplitude at the diaphragm. The excitation velocity at the diaphragm is determined to be 3.5 m/s. For incompressible flow, in Eq. (1), $U = U_J b/W = 0.8$ m/s, where U_J is the velocity amplitude of the synthetic jet, and W and b are the height of the diaphragm and the width of the jet orifice, respectively. Figure 3 shows that the amplitude of mass-flux at the slot is less than one-fourth of the amplitude of mass-flux at the diaphragm. This implies that the amplitude of velocity at the diaphragm is about 4 times 0.8 m/s, i.e., 3.2 m/s. This 2-D simulation assumes that the cavity is a cube. However, in the experiment, the cavity is actually a cylinder. Thus, the volume ratio of the cavity to the orifice is not the same in the computations as in the experimental setup. Therefore, it is expected that the velocity used in the simulation is not same as in the experiment.

Table 1 Computational mesh parameters

Zone	IMAX	JMAX	$\Delta x_{\min}$, mm	$\Delta x_{\max}$, mm	$\Delta y_{\min}$, mm	$\Delta y_{\max}$, mm
1	33	86	0.0212	0.746	0.00265	2.42
2	62	50	0.00691	0.105	0.00203	2.46
3	41	65	0.00691	0.0599	0.00415	0.598
4	197	139	0.00696	17.9	0.00409	46.9

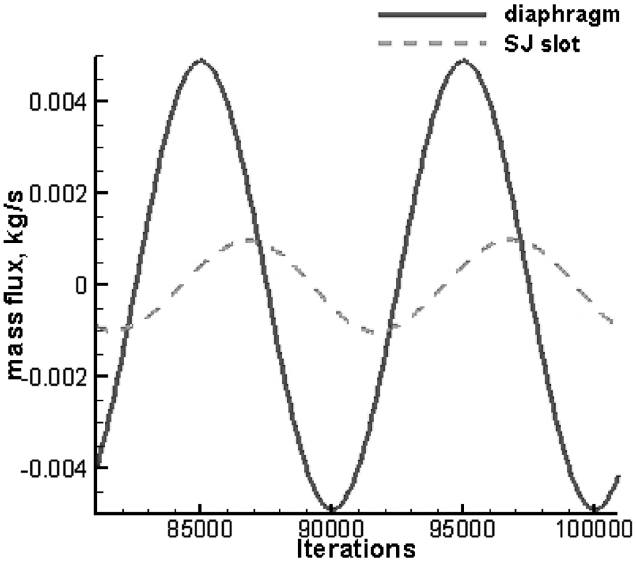

Fig. 3 Mass-flux at the diaphragm and across the slot.

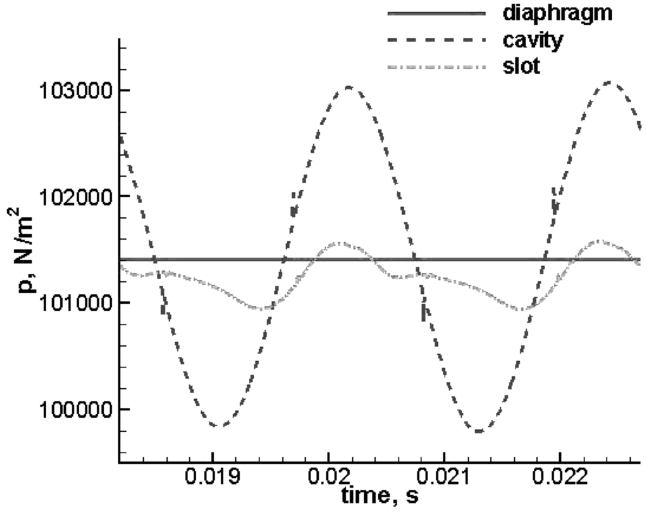

Fig. 4 Pressure variation at diaphragm, in cavity, and above the slot at $(x, y) = (0, 0.1$ mm).

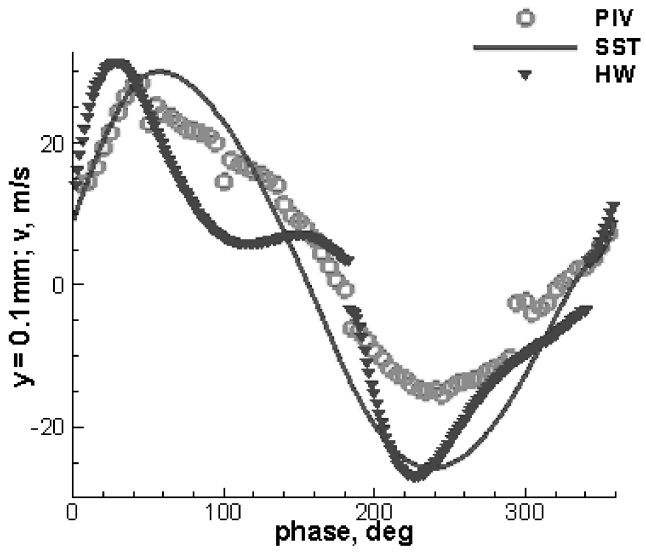

Fig. 5 v-velocity near the exit of the synthetic jet at $(x, y) = (0, 0.1$ mm).

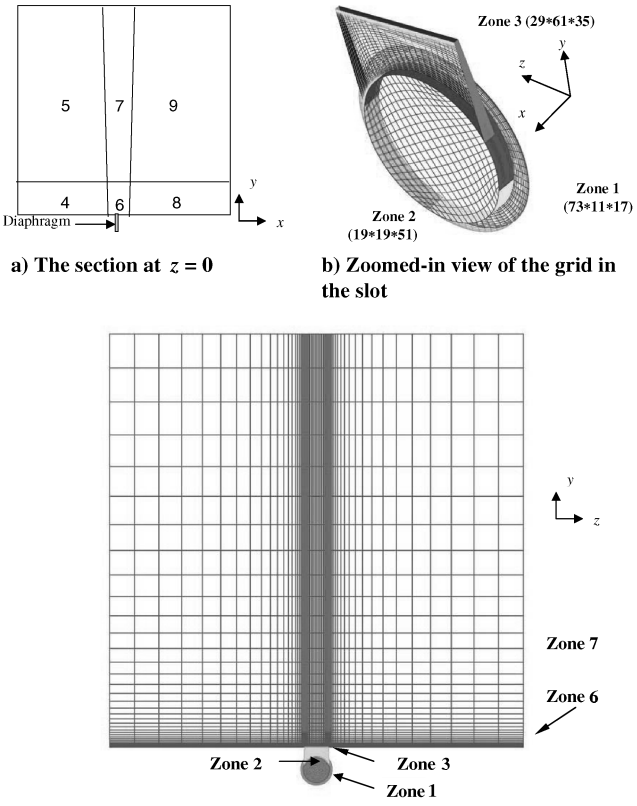

a) The section at $z = 0$

b) Zoomed-in view of the grid in the slot

c) The section at $x = 0$

Fig. 6 3-D grid used in the simulation.

Figure 4 shows the pressure variation with time at three locations: at the center of the diaphragm, at the center of the cavity on opposite side of the diaphragm, and at a location just above the jet slot at $(x, y) = (0, 0.1$ mm). In the experiment, the pressure inside the cavity varies between 99,702 and 102,667 Pa; it is between 99,771 and 103,080 Pa in the simulation. Figure 5 shows the calculated v-velocity at $(x, y) = (0, 0.1$ mm), which is in reasonable agreement with the particle image velocimetry (PIV) and hot-wire (HW) data in both phase and amplitude. The PIV measurement was obtained at $(x, y, z) = (0, 0.1224$ mm, $0)$, whereas the hot-wire measurement was taken at $(x, y, z) = (0, 0.1$ mm, $0)$, which may cause some difference in results. The uncertainty for the hot-wire measurement is $\pm 6\%$ near the solid surface (at a distance of 5 mm). The simulation and the experimental data are aligned at appropriate phase by using the guidelines provided in [14], where the phase is 340 deg when the velocity attains the average of the maximum and the minimum jet velocity at $(x, y, z) = (0, 0.1224$ mm, $0)$ in one period and is increasing in the PIV data. Figures 4 and 5 justify that the boundary conditions employed at the diaphragm are appropriate to simulate the conditions in the experimental setup, because the computed flow inside the cavity and at the slot behaves in a manner very similar to that in the experiment. These boundary conditions are similar to those employed by other CFDVAL2004 workshop participants.

Table 2 Computational mesh parameters for 3-D simulations

Zone	IMAX	JMAX	KMAX	$\Delta x_{\min}$, mm	$\Delta y_{\min}$, mm	$\Delta Z_{\min}$, mm
1	73	11	17	0.0612	1.66[a]	0.210
2	19	19	51	0.0612	1.66[a]	0.210
3	29	61	35	0.0612	0.00721	0.394
4/8	75	31	17	0.269	0.0277	0.394
5/9	75	25	17	2.87	3.91	0.394
6	75	31	71	0.0224	0.277	0.394
7	75	25	71	0.0418	3.91	0.394

[a]For zones 1 and 2, at section $x =$ constant, $\Delta y_{\min}$ are actually the arc lengths as seen in Fig. 6.

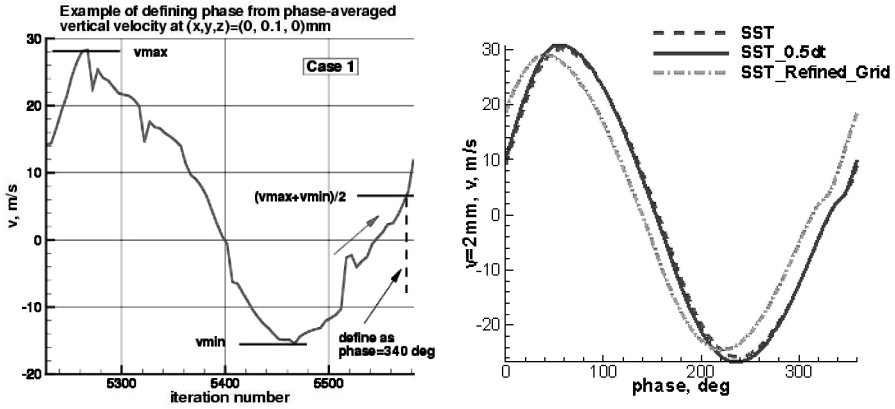

a) Velocity v of the synthetic jet at 340 deg phase in the experiment[14]

b) Computed history at (x, y, z) = (0, 2mm,0)
dt = time step = 0.22487 μs

Fig. 7 Velocity v history near the slot in the experiment and the computations.

However, the present work is the only one reported in the workshop, which ensures that the net mass-flux of the synthetic jet during one jet period is close to zero. This condition of zero net-mass-flux was achieved by painstaking calibration of appropriate pressure at the diaphragm.

C. 3-D Simulations: Mesh and Boundary Conditions

It should be noted that the authors of this paper are the only CFDVAL2004 participants who have performed the 3-D simulations for this case. Figure 6 shows the grid system used in the 3-D simulations. Table 2 shows the details of the zonal mesh. The grid has 9 zones and 534,977 grid points. The actuator cavity and the orifice are modeled as three zones, as shown in Fig. 6b. The external flow region was split into six zones to make the code run on four CPUs simultaneously. Jet orifice is located at zone 6. There are 29 points along the length of the slot (z-direction) and 35 points across the width of the slot (x-direction). In zone 6, where most significant changes in the flow take place, $\Delta x_{\min} = 0.0224$ mm, $\Delta y_{\min} = 0.0277$ mm, and $\Delta z_{\min} = 0.394$ mm. The y^+ for the first grid line above the wall is less than 2.5, which indicates that the grid resolution is sufficient in the y-direction for turbulent flow calculations.

The same type of pressure and velocity boundary conditions as described in Sec. III.B for 2-D simulations are generated and employed at the diaphragm for the 3-D simulations. The computed pressure and velocity amplitude at the diaphragm for 3-D simulations are 114,906 Pa and 4.1 m/s, respectively; these values were 101,419 Pa and 3.5 m/s, respectively in 2-D simulation. Again, the computed values of pressure and velocity for the simulation were obtained by iteration to satisfy the zero net mass-flux condition during one jet period and by matching the velocity at the slot to the experimental value. The reason for the slightly different values for pressure and velocity in 3-D simulation compared with 2-D simulation is due to the fact that the cavity geometries in the two simulations are different. In 2-D simulation, the cavity is assumed to be cubic; however, in actual reality in 3-D simulation, it is a cylinder.

IV. Simulation Results and Discussions

The results of 2-D and 3-D simulation are given in this section. The comparisons are made with particle image velocimetry and hot-wire measurements when available, which are obtained from the website of NASA Langley workshop [14]. All measurements were taken at the center plane ($z = 0$). All the computations were performed on a supercomputing platform at the Washington University Center for Scientific Parallel Computing (CSPC)[§] which has 64 R12000 MIPS processors with 400 MHz clock. The grids employed in the computations are shown in Fig. 6. The time step employed in the computations is dt = 0.22487 μs, which translates into 10,000 time steps per jet period for both 2-D and 3-D simulations. The range of Courant numbers in the simulations varies between CFL = 0.0011 and 4.35. For 2-D simulation, it requires about 5 h to calculate one SJ-period, running on a single CPU of CSPC cluster. 3-D simulations were performed using four CPUs in parallel. One jet period takes about 41 h of wall-clock time for a 3-D simulation. At least 10 jet periods are calculated to get a periodic solution. After that, two more periods are calculated to obtain output for post-processing.

First, the time step and grid independence studies were performed. The v-velocity history at (x, y, z) = (0, 2 mm, 0) is shown in Fig. 7b. The results are aligned according to the criteria shown in Fig. 7a [17]. It can be seen from Fig. 7b that reduction of time step by half shows little change in the velocity vs phase plot. However, doubling of the grid resolution in the external flow region in the y-direction results in a noticeable phase shift (about 10 deg) from the coarse grid calculations. It is difficult to match the phase at the slot exit exactly with the experimental data. By shifting the phase of the coarse grid velocity history by 10 deg to match the fine grid velocity history, the difference in simulations compared with the original coarse grid results was found to be negligible. Therefore the coarse grid (baseline mesh) in the y-direction was considered acceptable considering the additional computational requirements for fine grid calculations. Figure 8 shows the u-velocity contours at 45 deg phase in 2-D simulations obtained on the baseline mesh with time step dt and time step 0.5dt, and on the refined mesh with time step dt. The difference among these three calculations is insignificant. Thus we conclude that the solution is time-step independent as well as the baseline mesh is sufficient as mentioned before. In the following subsections, the "long-time-averaged" and "phase-averaged" results are presented as required by the workshop.

A. Long-Time-Averaged Flowfield

The instantaneous flowfield information is saved every 100 time steps, i.e., at every 3.6 deg during a jet cycle. It was found that the flowfield obtained by averaging 100 data files during one SJ-period and by averaging 400 data files during four jet periods were almost the same, after the solution was converged to a periodic state (which was obtained after 10–15 jet periods). So the long-time-averaged flowfield was obtained by taking average over one jet period (using 100 data files), after the solution had converged. Figure 9 shows the averaged v-velocity along the centerline y at ($x = 0$, $z = 0$) obtained by employing the SST, SST_LES, and SA turbulence models on a 2-D mesh, and SST and SA_LES (DES) turbulence models on a 3-D mesh along with PIV and HW measurements. It can be seen that along the centerline of the jet from $y = 2$ to 10 mm, both HW and PIV measurements of v-velocity are almost flat, whereas all the

[§]Data available on-line at http://harpo.wustl.edu/intro.html [cited 19 April 2004].

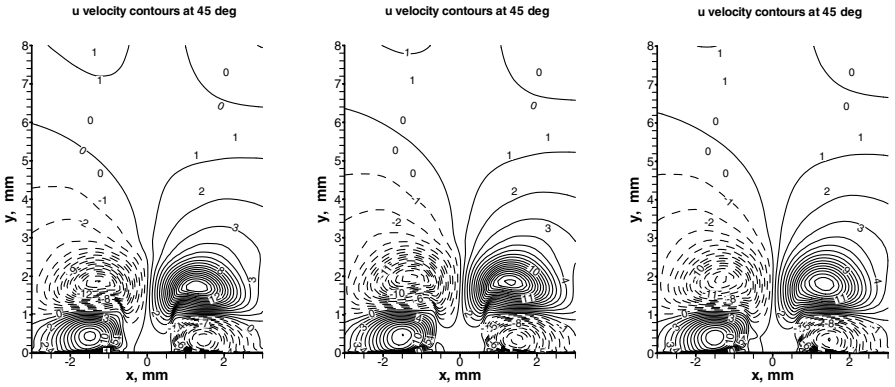

a) SST with baseline mesh and time step = dt b) SST with baseline mesh and time step = $0.5dt$ c) SST with refined mesh and time step = dt

Fig. 8 The u-velocity contours at 45 deg phase, $z = 0$.

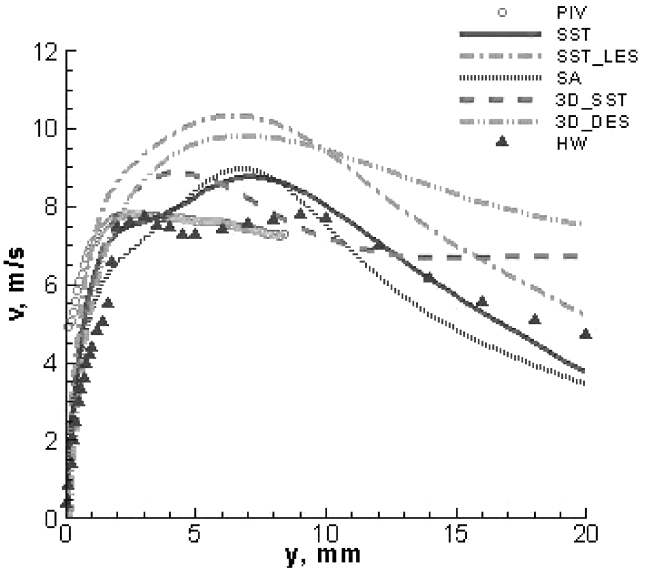

Fig. 9 Long-time-averaged v-velocity along the centerline y at ($x = 0$, $z = 0$).

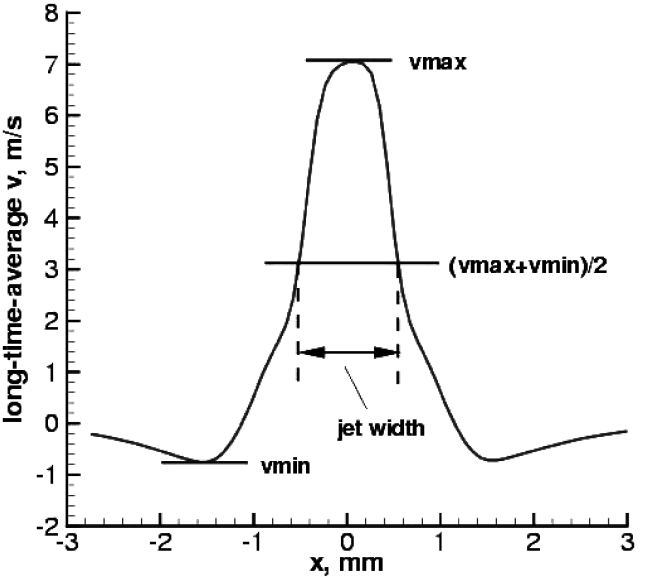

Fig. 11 Schematics employed in determination of jet width [17].

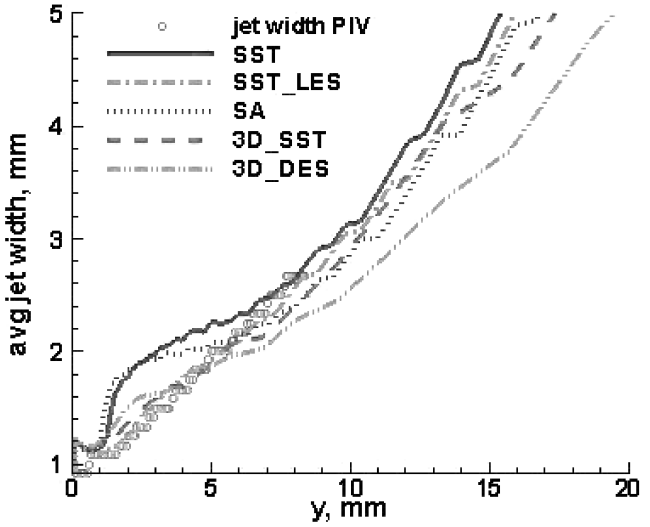

Fig. 10 Long-time-averaged jet width along the centerline y at ($x = 0$, $z = 0$).

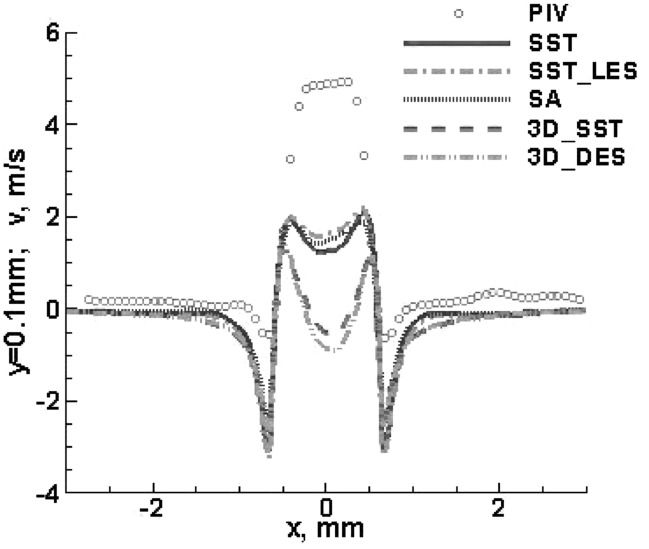

Fig. 12 Long-time-averaged v-velocity along x at $y = 0.1$ mm.

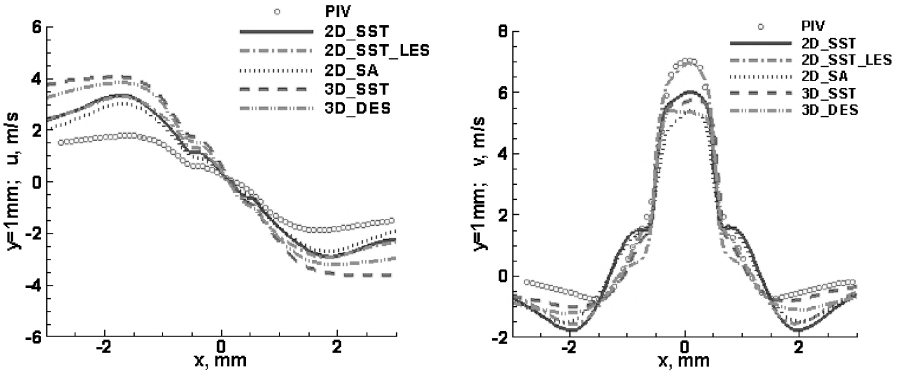

a) *u*-velocity along *x* b) *v*-velocity along *x*

Fig. 13 Long-time-averaged *u*- and *v*-velocity components along *x* at $y = 1$ mm.

simulations show peaks and then decay in the velocity profiles. The velocity profiles predicted by 2-D SA and SST models are similar, because they both are obtained using URANS with a phenomenological turbulence model. However, the velocity profile obtained with the 2-D SST/LES model is significantly different in peak as well as the decay, and is further away from the experimental data than the velocity profiles computed with URANS/SA and URANS/SST. Similar trends are observed comparing the 3-D SST and SA_LES (DES) approaches. The results of 2-D SST and SA models are closer to the experimental data than the 3-D SST and SA_LES (DES) model results. The differences between the 2-D and 3-D calculations using the same turbulence model can be attributed to the relatively coarser mesh employed in the 3-D simulations. However, there remains discrepancy between all the simulations and the experiment, which becomes pronounced far away from the jet. Similar behavior has been reported by all the workshop participants employing the URANS, and hybrid URANS/LES models. The spreading of the jet width is shown in Fig. 10; it is determined by using the method illustrated in Fig. 11 [14]. All the simulations give almost the same jet width at a distance 7 mm away from the jet exit except the 3-D SA_LES (DES) model. However, near the jet exit, 3-D SST model compares the best with the experimental data. 2-D URANS (with SST or SA model) predicts higher value of the jet width compared with the experiment, although both SST and SA models give almost the same results.

Figure 12 shows the *v*-velocity along *x* at $y = 0.1$ mm. All the simulations predict much lower value of *v* across the jet width (-0.635 mm $< x < 0.635$ mm). Our simulations have a *v*-velocity behavior similar to those of other simulations presented at the CFDVAL2004 workshop [14]. One of the reasons for this large difference between the computations and the experiment can possibly be attributed to the fact that the formulation of the boundary

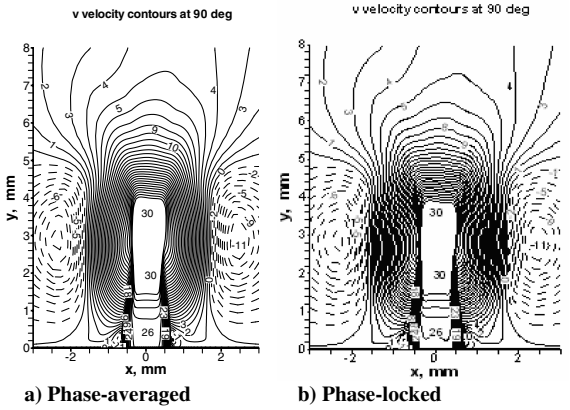

a) Phase-averaged b) Phase-locked

Fig. 14 Phase-locked and phase-averaged *v*-velocity contours at $\omega t = 90$ deg at $z = 0$.

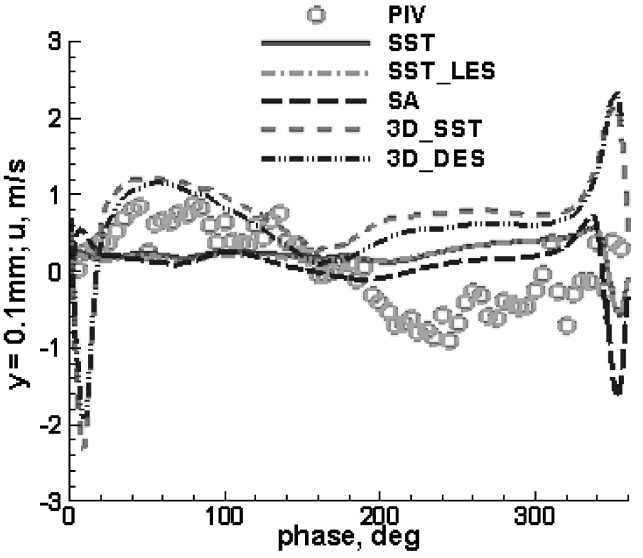

Fig. 15 Phase-averaged *u*-velocity at (0, 0.1 mm).

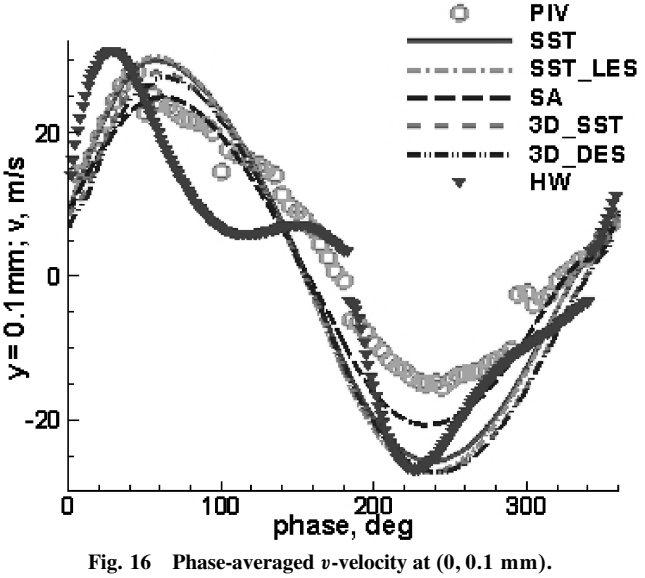

Fig. 16 Phase-averaged *v*-velocity at (0, 0.1 mm).

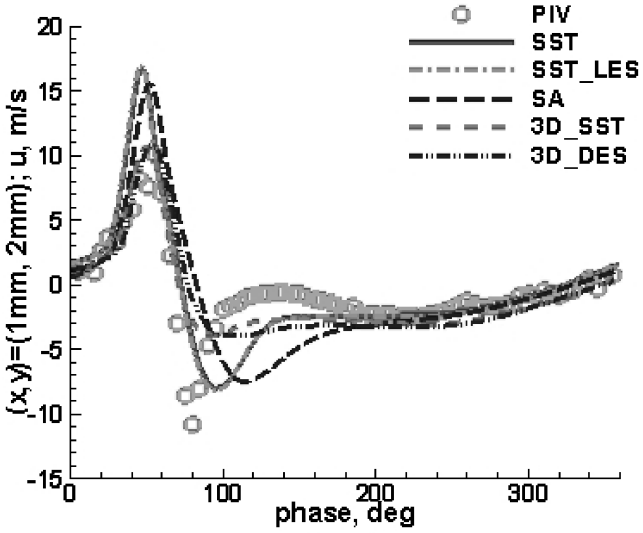

Fig. 17 Phase-averaged u-velocity at (1 mm, 2 mm).

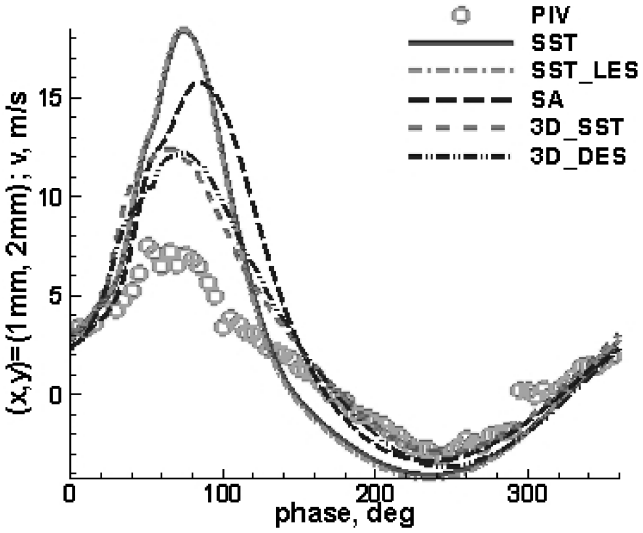

Fig. 18 Phase-averaged v-velocity at (1 mm, 2 mm).

condition at the diaphragm for the computations may not exactly simulate the situation in the experiment. The velocity profiles predicted by all 2-D simulations are very close to each other. Same holds for the 3-D simulations. As shown in Fig. 13, the difference between the v-velocity in the simulations and in the experiment becomes smaller at $y = 1$ mm.

B. Phase-Averaged Flowfield

Phase-averaged flowfield is calculated by averaging the flowfield at the same phase for different jet periods. Figure 14a shows the contours of v-velocity obtained by averaging the converged periodic solution over four different jet periods at 90 deg phase. It turns out that it is almost the same as the converged periodic phase-locked result obtained after 10–15 jet cycles as shown in Fig. 14b. We now present the computed phase-averaged results along with the phase-averaged PIV measurements in Figs. 15–18. Figures 15 and 16, respectively, show the variation of computed phase-averaged u- and v-velocity with phase at $(x, y) = (0, 0.1$ mm) and their comparison with phase-averaged experimental data. Figures 17 and 18, respectively, show the variation of computed phase-averaged u and v velocity with phase at $(x, y) = (1$ mm, 2 mm) and their comparison with phase-averaged experimental data. The simulation results agree qualitatively with the experiment. There appears to be no obvious advantage from the 3-D simulations near the jet exit. However, they do predict better agreement of (u, v) values with the experiment at $(x, y) = (1$ mm, 2 mm). Furthermore, there are no clear trends as to which turbulence model is superior.

V. Conclusions

Both 2-D and 3-D URANS simulations have been performed for case 1 of NASA Langley CFDVAL2004 workshop [14]. The employed boundary conditions and computed results are consistent with those of other workshop participants' approaches and results. Our work is unique among the workshop participants in two aspects: 1) The net mass-flux from the jet exit during one period was examined carefully. The appropriate pressure at the diaphragm was then determined such that the net mass-flux of the synthetic jet at the jet exit was very close to zero. 2) We are the only workshop participant who has performed the 3-D simulations; all other participants computed the 2-D case only. It can be concluded based on the computations presented in this paper and those performed by the other workshop participants that the overall agreement among the computations and measurements is not satisfactory; some flow variables are in reasonable agreement whereas several other differ significantly from the experimental data. Also, no particular turbulence model appears to be distinctly superior in prediction capability for this case [14]. Furthermore, 3-D simulations do not appear to improve the correlation with experimental data, which is expected because the measurements were taken in the center plane of the rectangular slot jet of aspect ratio 28.

Acknowledgments

The authors thank the Washington University Center for Scientific Parallel Computing (CSPC) for providing the computing hardware and the Boeing Co. for providing the software package used in this work. Special thanks are due to Andrew W. Cary of Boeing for help with the grid generation code ZONEI3G and the URANS solver WIND. The authors are grateful to the referees for constructive comments, which have improved the paper.

References

[1] Kral, L. D., Donovan, J. F., Cain, A. B., and Cary, A. W., "Numerical Simulations of Synthetic Jet Actuators," AIAA Paper 97-1284, June 1997.

[2] Kral, L. D., and Guo, D., "Characterization of Jet Actuators for Active Flow Control," AIAA Paper 99-3573, June–July 1999.

[3] Guo, D., Cary, A. W., and Agarwal, R. K., "Numerical Simulation of the Interaction of Adjacent Synthetic Jet Actuators," *Proceedings of the International Conference on Computational Fluid Dynamics (ICCFD2)*, edited by S. Armfield, P. Morgan, and K. Srinivas, Springer–Verlag, Berlin, 2003, pp. 560–565.

[4] Guo, D., Cary, A. W., and Agarwal, R. K., "Numerical Simulation of Vectoring Control of a Primary Jet with a Synthetic Jet," AIAA Paper 2002-3284, June 2002.

[5] Smith, B. L., and Glezer, A., "The Formation and Evolution of Synthetic Jets," *Physics of Fluids*, Vol. 10, No. 9, 1998, pp. 2281–2297.

[6] Smith, B. L., Trautman, M. A., and Glezer, A., "Controlled Interactions of Adjacent Synthetic Jets," AIAA Paper 99-0669, 1999.

[7] Lee, C. Y., and Goldstein, D. B., "Two-Dimensional Synthetic Jet Simulation," *AIAA Journal*, Vol. 40, No. 3, 2002, pp. 510–516.

[8] Mittal, R., Rampunggoon, P., and Udaykumar, H. S., "Interaction of a Synthetic Jet with a Flat Plate Boundary Layer," AIAA Paper 2001-2773, 2001.

[9] Cui, J., Agarwal, R., Guo, D., and Cary, A. W., "Numerical Simulations of Behavior of Synthetic Jets in Cross-Flow," AIAA Paper 2003-1264, 2003.

[10] Rizzetta, D. P., Visbal, M. R., and Stanek, M. J., "Numerical Investigation of Synthetic Jet Flowfields," *AIAA Journal*, Vol. 37, No. 8, 1999, pp. 919–927.

[11] Smith, B. L., and Glezer, A., "Vectoring and Small-Scale Motions Effected in Free Shear Flows Using Synthetic Jet Actuators," AIAA Paper 97-0213, 1997.

[12] Lee, C. Y., and Goldstein, D. B., "Simulation of MEMS Suction and Blowing for Turbulent Boundary Layer Control," AIAA Paper 2002-2831, June 2002.

[13] Kotapati, R. B., and Mittal, R., "Time-Accurate Three-Dimensional Simulations of Synthetic Jets in Quiescent Air," AIAA Paper 2005-103, Jan. 2005.
[14] Gatski, T., and Rumsey, C., "CFD Validation of Synthetic Jets and Turbulent Separation Control," NASA Langley Research Center Workshop, March 2004, http://cfdval2004.larc.nasa.gov [cited 19 April 2004].
[15] Ahmed, A., and Bangash, Z., "Axi-Symmetric Coaxial Synthetic Jets," AIAA Paper 2002-0269, Jan. 2002.
[16] Zaman, K., and Milanovic, I., "Synthetic Jets in Cross-Flow, Part 1: Round Jet," AIAA Paper 2002-3714, June 2002.
[17] Milanovic, I., and Zaman, K., "Synthetic Jets in Cross-Flow, Part 2: Jets from Orifices of Different Geometry," AIAA Paper 2002-3715, June 2002.
[18] Honohan, A. M., "The Interaction of Synthetic Jets with Cross Flow and the Modification of Aerodynamic Surfaces," Ph.D. Dissertation, School of Mechanical Engineering, Georgia Institute of Technology, Atlanta, May 2003.
[19] Bush, R. H., "The Production Flow Solver of the NPARC Alliance," AIAA Paper 88-0935, 1988.
[20] Wilcox, D. C., *Turbulence Modeling for CFD*, 2nd ed., DCW Industries, La Canada, CA, 2000.
[21] Spalart, P. R., Jou, W. H., Strelets, M., and Allmaras, S. R., "Comments on the Feasibility of LES for Wings, and on a Hybrid RANS/LES Approach," *Advances in DNS/LES*, edited by C. Liu and Z. Liu, Greyden Press, Columbus, OH, 1997.
[22] Mani, M., and Bush, R. H., "A Two-Equation Large Eddy Stress Model for High Sub-Grid Shear," AIAA Paper 2001-2561, 2001.
[23] Spalart, P. R., and Allmaras, S. R., "A One-Equation Turbulence Model for Aerodynamic Flows," AIAA Paper 92-0439, 1992.
[24] Menter, F. R., "Zonal Two-Equation k–ω Turbulence Models for Aerodynamic Flows," AIAA Paper 93-2906, 1993.
[25] Speziale, C. G., "Turbulence Modeling for Time-Dependent RANS and VLLES: A Review," *AIAA Journal*, Vol. 36, No. 2, 1998, p. 173.
[26] Romer, W. W., and Bush, R. H., "Boundary Condition Procedures for CFD Analyses of Propulsion Systems—The Multi-Zone Problem," AIAA Paper 93-1971, 1993.

K. Ghia
Associate Editor